Research Square

Preprints are preliminary reports that have not undergone peer review.
They should not be considered conclusive, used to inform clinical practice,
or referenced by the media as validated information.

Emphasizing the structural and computational characterisation of an HIV-1 IN binding interface against potential inhibitors for a promising drug strategy

Adeniyi Thompson Adewumi
University of South Africa
Sekele Tshepo Lucas
University of South Africa
Salerwe Mosebi
mosebs@unisa.ac.za

University of South Africa

Research Article

Keywords: HIV-1 viral integrase, Allosteric site, Structural and functional dynamics, inhibitory mechanisms, drug design

Posted Date: March 9th, 2026

DOI: https://doi.org/10.21203/rs.3.rs-8984808/v1

License: This work is licensed under a Creative Commons Attribution 4.0 International License.
Read Full License

Additional Declarations: No competing interests reported.

Abstract

HIV/AIDS has remained a deadly and incurable human disease. The current strand transfer inhibitors (INSTIs), such as raltegravir (RAL), face drawbacks, including a low genetic barrier to resistance and potential cross-resistance. The design of small-molecule antivirals targeting the integration step of the viral life cycle has been the recent highlight of the IN allosteric inhibitor (INLAIs) strategy. This interventive approach has been potentiated by recently developed chromane-functionalised compounds: BDM-2/INH1, MUT871/INH2, and MUT872/INH3, which exhibit therapeutic activity at the IN interface. Therefore, we investigated the conformational changes of HIV-IN and the dynamical events underlying the antiviral mechanism of the compounds upon binding to the IN allosteric interface using an integrated all-atom molecular dynamics simulation. Time-scale dynamical findings showed that the compounds induced structural changes in the protein. Moreover, the inhibitor-bound systems showed insignificant differences in the structural flexibility (mean RMSF, Å: 1.50, 1.50, 1.60, 1.30, 1.40) and the atomistic motion (mean RMSD, Å: 2.57, 2.28, 2.23, 2.33, 2.56) compared to the unbound protein within the conformational space, respectively. Trajectory investigations into the binding site indicate that compounds INH1 (–25.27 kcal/mol) and INH3 (–25.26 kcal/mol) exhibited mechanistic transitions within the interface, as evident in their high-energy interactions at the allosteric binding site. Thus, the proposed inhibitors are comparable to RAL (–27.50 kcal/mol), except for INH2 (–13.19 kcal/mol). These findings present a model that describes the structural behaviour and the mechanism by which INLAI inhibitors can interact with IN to enhance their development during clinical trials.

INTRODUCTION

Human immunodeficiency virus (HIV) is a global disease; about 1.3 million individuals (44% women and girls) are disproportionately estimated to have acquired HIV, and 39.9 million people are living with HIV, as UNAIDS 2024 reported [1]. As of 2023, it was reported that an estimated 42.3 million individuals have died from HIV/AIDS-related illnesses since the onset of the epidemic. The HIV epidemic is still challenging because the goals to decrease new infections and deaths by 75% in 2020 and 90% by 2030 are far from being achieved. The number of new infections has decreased by only 60% since its peak in 1995, as of 2023 [2][3]. In 2023, the World Health Organisation (WHO) reported that there were 25.6 million (20.8 million in East and Southern Africa and 4.8 million in West and Central Africa) people with HIV (WHO, 2022). South Africa has the highest number of people (above 8 million people as of 2024 and 12.8% of the population) living with HIV globally, while Eswatini and Lesotho have higher adult HIV prevalence rates [4][5][6]. However, South Africa has made significant strides in reducing new infections and AIDS-related deaths through expanded treatment programs [7]. Despite this progress, new infections continue to occur, particularly among young adults [8].

HIV belongs to a family of retroviruses classified as HIV-1 and HIV-2, which cause an incurable disease currently managed by antiretroviral therapies (ARTs), but the treatment must be lifelong, as a total cure from the infection has not yet been established [9][10]. Inability to suppress or maintain replication of HIV viral load below 200 copies/ml) The emergence of resistant strains has resulted from the

widespread use of these ARTs [10]. Despite combined Antiretroviral Therapies (cARTs), multidrug-resistant strains continue to emerge and are also associated with increased risks of disease progression and death rate. The most recent drug (Lenacapavir) capsid inhibitor, is a long-acting antiretroviral drug, administered twice a year as a subcutaneous injection, demonstrating a small margin of resistance during clinical trials [11]. Lenacapivir resistance mutation has been identified in 5/8 patients after 3 weeks of lenacapavir monotherapy [12][13]. An essential step in the replication of retroviruses is the integration of a double-stranded DNA copy of their RNA genome into the host cell chromosome during the replication cycle, catalysed by the integrase enzyme, making it an attractive target for therapy [14] [10].

HIV integrase (IN) is a 32 kDa protein that is essential in the integration of viral DNA (vDNA) into the host cell's chromosome [10]. It consists of three recognised domains: N-terminal zinc binding (amino acids 1–50), a catalytic core domain (amino acids 50–212), and the DNA-binding C-terminal domain (amino acids 212–288) [14][15][10]. The integration of HIV DNA is achieved via two reaction steps, and the first is the removal of the terminal GT dinucleotide from each viral end, leaving the CA dinucleotide with a free 3' hydroxyl group and an overhanging 5' AC on the complementary strand, referred to as the 3' processing[16]. The second step involves cleaving the host DNA, followed by a series of phosphodiester transesterification reactions to incorporate the 3' ends of the vDNA into the host DNA at the 5' end, termed the strand transfer reaction [17] [15]. HIV-1 strand transfer inhibitors (INSTIs) are a class of antiretroviral drugs for HIV, including the first-generation INSTIs: raltegravir (RAL) and elvitegravir (EVG), and the second-generation INSTIs: dolutegravir (DTG), bictegravir (BIC), and carbotegravir (CAB) [18]. Mechanism of action of INSTIs includes (1) blockage of IN active site, thereby inactivating the intasome (complex of IN and viral DNA) and dislocating the vDNA 3' terminal end; and (2) inhibition of the insertion of vDNA into the host chromosome as they prevent formation of a covalent bond between the vDNA and host DNA [19][20]. Resistance to the currently FDA-approved INSTI, including RAL, EVG, BIC, DTG, and CAB, has been reported. Specific side effects include severe skin reactions, diarrhoea, tiredness, concerns about birth defects, and fatigue [21][10][20][22].

Due to resistance to the INSTIs, side effects, and high cost of treatment, it is crucial to continue researching alternative compounds targeting the HIV pandemic. LEDGF/p75 has been implicated in other human diseases, like acute myeloid leukaemia [23][24], and its role in HIV replication has been shown as the main chromatin-tethering factor for IN [25]. LEDGF/p75 binds to IN via its C-terminal integrase binding domain while interacting with chromatin via its PWWP domain in the N-terminal [26] [25]. Inhibitor activity against integrase (IN) substrate-binding involves compounds that interfere with the HIV integrase enzyme's ability to integrate viral DNA into the host cell. This inhibition can occur through several mechanisms, including: blocking the active site to prevent strand transfer (integrase strand transfer inhibitors, INSTIs), disrupting the formation of the required multi-protein complex by binding to allosteric sites (Allosteric Integrase Inhibitors, ALLINIs), or competing directly with the viral DNA substrate for binding to the integrase complex [18]. Competitive blocking or preventing the binding of LEDGF/p75 gives rise to another class of IN inhibitors: non-catalytic site integrase inhibitors (NCINIs),

multimerisation integrase inhibitors (MINIs), IN-LEDGF allosteric inhibitors (INLAIs), and allosteric IN inhibitors (ALLINIs).

Among the reported small-molecule INLAIs are STP0404 (Pirmitegravir), BDM-2, and benzylindoles, such as benzodioxole-4-carboxylic acid and 8-hydroxyquinoline, which were identified using *in silico* methods [27][21][28]. The BDM analogues engage the substrate-binding and allosteric-binding sites in a series of crystal structures of the HIV-1 IN catalytic core and C-terminal domains. Inhibitor activity prevents or blocks substrate binding. However, inactivity has also been reported due to certain factors, such as drug or drug candidate resistance. Moreover, a recent study by Bonnard *et al* showed that the allosteric-binding (non-catalytic) site of HIV-1 IN was targeted with BDM derivatives, including BDM-2, MUT871, and MUT872 [29]. BDM-2 and its analogue inhibitors demonstrated good inhibitory concentration (IC_{50}) of activity of 0.047 ± 0.014, 0.014 ± 0.005, and 0.17 ± 0.02, respectively [21]. Moreover, the authors reported various interactions between the HIV-1 IN allosteric site and the BDM-2 series using the HTRF-based assays. The molecular mechanisms of action of the INLAI BDM-2 derivatives upon binding to the HIV-1 IN allosteric binding site and the overall impact on the structure and function of the target have not been fully understood. In addition, several reports have shown that experimental studies of protein encounter limitations, such as difficulties with dynamics and disordered proteins, as well as potential artefacts.

Computational techniques, including molecular docking and molecular dynamics simulations, have been used in drug discovery because they reduce time and cost [30]. Combined MD simulations and MMGB(PB)SA binding free energy calculation method are rapid, and offer dynamic insights at an atomic level, and can provide insights into conformational changes and binding landscapes beyond experimental reach. This is especially true given recent advances in the discovery of force fields that overcome limitations, such as the accurate simulation of explicit solvent effects and protein-protein interactions. This study investigated the characteristic motion and dynamics of the structure and function of the whole HIV-1 IN CCD-CTD and its binding landscape, using integrated molecular dynamics simulations. Moreover, the mechanistic actions of BDM-2, MUT871, and MUT872 were determined using the MMGB(PB)SA method.

METHODOLOGY

2.1 Ligand selection and preparation

The chemical structures of BDM-2 (INH1), MUT871 (INH2), MUT872 (INH3), and reference inhibitor raltegravir (RAL) were downloaded from the PubChem database in structure data files (SDF) format, accessed on 30/07/2024, while the unavailable structures in the database were drawn using ChemAxon Marvin Suite 18.10, 2017 (http://www.chemaxon.com/). Using a previously described protocol, the ligands were optimised and prepared with the UCSF Chimera [31][32], which was used to add hydrogen and Gasteiger charges using the antechamber modules. Furthermore, the prepared ligands were saved as PDBQT files using the AutoDock Tools [33]. An appropriate number of polar hydrogen atoms was

added to the system. Figure 1 shows the chemical structures of BDM-2 (a), MUT871 (b), MUT872 (c), and RAL (d).

2.2 Protein retrieval and preparation

The human immunodeficiency virus integrase (HIV-IN) protein (PDB ID: 8BV2) was obtained from the RCSB Protein Data Bank format [21]. The protein is co-crystallised with a ligand (RWR) 2S-2-[3-cyclopropyl-2-(3,4-dihydro-2H-chromen-6-yl)-6-methyl-phenyl]-2-[(2-methylpropan-2-yl)oxy] ethanoic acid. The chosen structure was solved by X-ray crystallography and has a resolution of 2.00 Å. Afterwards, the protein was prepared by removing all nonstandard molecules, such as water, sulfate ions, and magnesium ions, and subsequently adding hydrogen using the UCSF Chimara tool.[31].

2.3 Molecular docking

The inhibitors RWR (co-crystallised ligand), BDM-2, MUT871, MUT872, and RAL (standard drug) were selected for docking at the allosteric site of HIV-1 subtype B. A redocking study was conducted to evaluate the ability to reproduce the co-crystallised binding geometry and orientation of the associated ligand in a rigid macromolecular state using AutoDock Vina [34]. Re-docking also evaluates the testing of ideal docking parameters for the HIV-IN subtype B structure. On the other hand, docking of the study ligand was performed using the same procedure with the software's default settings. A grid box for the allosteric site was generated using AutoDock Vina functionality in the AutoDock Tool (ADT) [35][36]. The coordinates of the gridbox size (Å) and the centre (Å) parameters for HIV-1 subtype B were x(58, 34.384), y(52, -29.386), and z(44, -27.04), respectively. This is to differentiate ligands based on their binding geometries to the allosteric site of the HIV-IN CCD-CTD protein [37][38][39]. Each IN-inhibitor binding was set to consist of eight exhaustive conformations. (Tanchuk et al., 2015). The ligands were docked to the HIV-1 IN allosteric site using the AutoDock Vina algorithm, keeping the HIV-1 IN protein rigid. AutoDock Vina provided results in the pdbqt format, and the optimal geometric conformation that has the best binding energy was chosen from the ViewDock feature on UCSF Chimera, saved in complex with each ligand and visualised by uploading the complexes on BIOVIA Discovery Studio 4.5 (DS) [40]. Subsequently, the docking complexes were prepared for MD simulations.

2.4 Molecular dynamics simulations

Molecular dynamics (MD) provides a platform to study the dynamics of a protein binding to a ligand or other partners, such as a small molecule compound, an aptamer, a peptide, or another protein [41][42][43]. Critical insights into the mechanism of biological processes are often gained through MD simulations by computing differences in binding free energy. This technique can also reveal information about the system stability, conformational changes, and fluctuations of ligand-bound and unbound protein structures during docking or MD simulations [40]. It explores the biophysical properties of molecules to study proteins extensively for drug discovery and development [44].

Before the MD simulations, the receptor IN, the inhibitors, the co-crystal ligand, and the standard drug RAL were prepared from each docked-ligand complex with the most negative binding score. The MD

simulations were performed using the accelerated GPU version of PMEMD in the AMBER18 package (http://www.chpc.ac.za/index.php/resources/lengau-cluster) on the Lengau CHPC server [45][46]. The FF14SB force field of the Amber package was used to define the HIV-1 protein parameters. The protein was modified, renamed, and protonated (histidine) using an in-house *pdb4amber* script, which was followed by the generation of topology and parameter files for the respective HIV-1-bound ligand complexes [47]. ANTECHAMBER was used to generate atomic partial charges for the ligands by using the Restrained Electrostatic Potential (RESP) and the General Amber Force Field protocols [48][49]. The Leap module of Amber 18 allowed the addition of hydrogen atoms to the systems and of Na + and Cl- counter ions for neutralisation. Each system was implicitly suspended within an orthorhombic box of TIP3P water molecules to ensure that all atoms were within 12 Å of any box edge [50][51][52][53]. An initial minimisation of 2500 steps was performed with a restraint potential of 500 kcal/mol Å2 applied to all complexes and the unbound system. Subsequently, a full energy minimisation of 5000 steps was performed using the conjugate gradients algorithm without restraints.

The systems were individually and gradually subjected to 50 ps MD simulations from 0–300 K to maintain a fixed number of atoms and fixed volume, indicating a canonical ensemble (NVT). The system's solutes are imposed with potential harmonic restraint of 10 kcal/mol*Å2 and collision frequency of 1.0 ps $^{-1}$. Next, an equilibration of 1 ns for each system was conducted, keeping the operating temperature at 300 K and the number of atoms and pressure constant, mimicking an isobaric–isothermal ensemble (NPT). The system's pressure was maintained at 1 bar using the Berendsen barostat. Each MD simulation was run for 310 ns, using the SHAKE algorithm to constrain hydrogen bonds [54][55]. The simulation time step was 2 fs, and a single-precision/fixed-precision (DPFP) model was used. The simulations were performed in an isobaric–isothermal ensemble (NPT), with randomised seeding, a constant pressure of 1 bar maintained by the Berendsen barostat [56][57], a pressure-coupling constant of 2 ps, a temperature of 300 K, and a Langevin thermostat with a collision frequency of 1.0 ps − 2. Coordinates were saved every 1 ps, and the trajectories were analysed at the same interval using the PTRAJ module [58] in Amber18. Lastly, the MicroCal Origin 6.0 software [59] was used to plot and analyse the data.

2.5 Post molecular dynamics simulations analysis

Computational metrics, including the root mean square deviation (RMSD)[60], the root mean square fluctuation (RMSF)[61], the radius of gyration (RoG), the principal component analyses (PCA), the binding free energies (MM/GBSA)[62], and the per-residue energy decompositions (PRED)[63][64] were calculated by analysing the trajectories of each system using the PTRAJ module in AMBER 18/GPU. The BIOVIA Discovery Studio packages were used for visualisation, structural, and interaction analyses, while plots and statistical values were produced with the Origin 6 MicroCal Program [59].

2.5.1. Binding free energy (BFE) calculations

The binding free energies (BFE) of the receptor-ligand systems were calculated from 15 snapshots spanning 310 ns of simulation trajectories to provide further insights into the binding mechanisms of the

promising HIV-1 IN inhibitors, compared with affinities obtained from molecular docking calculations. Therefore, we used molecular mechanics/generalised Born surface area (MMGBSA) methods to determine binding free energies, with the systems completely stripped of added solvents. The following are the calculation formulas:

$\Delta G_{bind} = \Delta G_{complex} - \Delta G_{receptor} - \Delta G_{ligand}$ ..... (**i**)

$\Delta G_{bind} = E_{gas} + G_{solvent} - T\Delta S$ ..... (**ii**)

$E_{gas} = E_{int} + E_{vdw} + E_{ele}$ ..... (**iii**)

$G_{sol} = G_{GB} + G_{SA}$ ..... (**iv**)

$G_{SA} = {}_{\gamma}SASA$ ..... (**v**)

Where ΔG_{bind} represents gas-phase summation, E_{gas} is the gas-phase energy, G_{sol} denotes the free solvation energy, and $T\Delta S$ is the entropy. E_{int}, E_{ele}, and E_{vdw} denote the internal, electrostatic, and van der Waals energies, respectively. E_{gas} was estimated using the AMBER FF14SB force field. Energy contributions of polar and non-polar states account for G_{sol}. S denotes the total entropy of the system, which was calculated using the Normal mode analysis incorporated in AMBER Tools, and T is the temperature. The MM/GB(PB)SA method in AMBER18, with per-residue energy decomposition (PRED) at the atomic level, was used to quantify each residue's contribution to the total BFE at the active site. Moreover, the calculated energies were utilised over 40,000 frames from the 310 ns trajectories. The MM/GB(PB)SA protocol requires completely removing the used solvent and replacing it with a dielectric continuum.

Furthermore, the Per-residue energy decomposition (*PRED*) analysis was performed to estimate individual energy contributions from interacting residues within the HIV-1 IN allosteric binding pocket. The PRED analysis explains the amount of energy each amino acid or residue donates to the total binding free energy of the inhibitors.

2.5.2 Integrase-Inhibitor interactions

The ligand interaction add-on in BIOVIA Discovery Studio (DS) was utilised to determine interactions between the study inhibitors and the IN allosteric pocket amino acids. Several snapshots were generated at various times within 310 ns MD simulation trajectories to identify the interactions and to understand the molecular forces between the IN CCD-CTD interface receptor and inhibitors.

2.5.3 Root mean square fluctuation

Root Mean Square Fluctuation (RMSF) is a valuable molecular dynamics (MD) simulation tool for understanding protein flexibility and dynamics. It quantifies the average deviation of individual atoms from their mean positions over time, revealing which regions of the protein are most flexible and which are more rigid. RMSF can be compared between different protein structures (e.g., unbound or holo

forms) to understand how ligand binding or other factors affect protein flexibility. In essence, RMSF provides a detailed map of protein flexibility, which is crucial for understanding how proteins function, interact with other molecules, and adapt to different environments.

RMSF is computed as follows:

$$\mathrm{sRMSF}_i = \frac{(\mathrm{RMSFi} - \bar{\mathrm{RMSF}})}{\sigma \mathrm{RMSF}}$$

..... (**vi**)

$RMSF_i$ represents the i^{th} residue RMSF from which the average RMSF is subtracted, which is divided by the standard deviation of the RMSF [σ(RMSF)] to equal the standardised RMSF [s(RMSFi)].

2.5.4 Radius of Gyration (ROG)

This measures protein compactness and stability during simulation; a non-significant change in ROG over time indicates better protein stability [65]. The equation below is the expression of a calculation formula:

$$r^2 gyr = \frac{\left(\sum_{i-1}^{n} W_i \left(r_i - \bar{r}\right)^2\right)}{\sum_{i-1}^{n} w_i}$$

..... (**vii**)

Where equation terms include the position of the i^{th} atom (r_i), mass/weight of each atom (W), and the centre of mass of atom i (r). The mean values of ROG were calculated by taking the values over the number of frames in each trajectory [66].

RESULTS AND DISCUSSION

3.1 Molecular docking analysis

Reports have revealed that there is a non-catalytic (allosteric) pocket of the HIV-1 integrase located between the HIV-1 IN CCD dimer and the CTD interface, and the primary active site, i.e., the catalytic core domain, where the catalytic reactions occur (Bonnard et al., 2018; Burlein et al., 2017; Wielens et al., 2010). This non-catalytic site has been identified as interacting with INLAIs and LEDGF/p75. Thus, the pocket is known as the INLAI-induced HIV-1 IN CCD dimerisation-CTD interface. The HIV-1 IN allosteric pocket comprises of CCD amino acid residues LEU102, THR124, THR125, ALA128, ALA129, TRP132, GLN168, ALA169, GLU170, HIS171, THR174, MET178 and CTD amino acid residues TYR226, TRP235,

LYS266, and ILE268. Figure 2a shows the HIV-1 IN CCD-CTD active pocket residues; colour online: yellow green (CCD), brown (CTD).

The CCD dimer-CTD interface is a well-characterised binding pocket that has been reported to accommodate INLA inhibitors. Therefore, we explore the binding of three newly reported INLAI BDM-2 analogues for the energetically most favourable HIV-1 IN CCD-CTD interface. The inhibitors ligands (Co-crystal RWR, RAL, BDM-2, MUT871, and MUT872) interact with the HIV-1 IN CCD-CTD interface at various levels of binding affinities. The BA and the root mean square deviation (RMSD) of the best pose of the re-ligand were 5.5 kcal/mol and 0.0000 Å, respectively.

Table 1 **shows t**he binding affinities (BA) of the ligands for the protein, ranging from − *6.*8 to − *5.*8 kcal/mol, with INH2 having the highest value, followed by INH1 and INH3, and raltegravir (standard drug) having the highest. However, the binding energies differ by 1 kcal/mol, indicating that the docking scores do not differ significantly between INH1 and INH3. Moreover, the docking RMSD values for the inhibitors were 0.0000 Å, an ideal value. Comparatively, the RMSD values indicate that the co-ligand redocked to the active site and is stable, thereby validating that the docking protocol adequately replicates the experimental structure data. In addition, the results showed that the docking parameters (grid box size, exhaustiveness = 8, and scoring function) are reliable for predicting native-like poses. Finally, the superimposed structures (Fig. 2b) of the re-docked ligand and co-crystal conformer indicate good stability.

Moreover, an *in vitro* study showed MUT871 (INH2) to be a potent inhibitor with a 50% inhibitory concentration (IC_{50}) of 14 nM, while MUT872 and BDM-2 yielded IC_{50} values of 17 nM and 47 nM, respectively [21].

Table 1
The binding affinities for the allosteric integrase inhibitors.

Ligand	PubChem Synonym	Docking score (kcal/mol)
INH1	BDM-2	-5.8
INH2	MUT871	-6.5
INH3	MUT872	-5.8
RAL	Raltegravir	-6.8
RWR	Co-crys lig	-5.5

BDM-2 and MUT871 contain the carboxyl and tert-butoxy groups, respectively, while MUT872 has the tert-butoxy group replaced by a more compact cyclopropyloxy group, which allows sufficient space to accommodate the Ile side chain, suggesting the good binding energies shown by the three compounds against HIV-1 IN. Most of the BDM-2 series of INLAIs appeared to inhibit the interaction between full-

length HIV-1 IN and LEDGF/p75 with higher potency than the interaction between the respective binding domains (NTD, CCD, and CTD).

3.2 Molecular Dynamics (MD) Simulations

3.2.1 Thermodynamics analysis

The binding affinities calculated for HIV-1 IN-ligand complexes using the MMGB(PB)SA-based calculations are summarised in Table 2, where the total free binding energy (ΔGbind) ranges from RAL > INH1 > INH2 > INH3. While RAL has a prominent value of − 27.50 kcal/mol, INH1 and INH2 have similar values of − 25.27 ± 0.24 kcal/mol and − 25.26 ± 0.16 kcal/mol, respectively. The high negative energy (ΔG) values of INH1 and INH3 can be attributed to their high van der Waals energy (E_{vdW}): − 30.78 kcal/mol and − 30.84 kcal/mol, respectively. While INH2 ranked high in binding affinity in the molecular docking study, it had the lowest binding free energy, − 13.19 kcal/mol. This could be because of its low average van der Waals energy value − 17.22 kcal/mol, compared with other inhibitors. The results suggest that van der Waals and electrostatic interactions contribute to the binding of the inhibitor ligands. The high binding energy values of INH1 are supported by the 50% effective concentrations (EC_{50}). Although RAL (standard drug) has a higher binding free energy (–27.50 ± 0.14), the drug has been confronted with the development of drug resistance, particularly in treatment-experienced patients and in cases of virological failure [67][68][69]. The resistance can emerge due to factors like inconsistent adherence, inadequate drug levels, or pre-existing resistance mutations. Moreover, specific drug interactions, particularly with antacids, can reduce raltegravir's efficacy by affecting its absorption [70][71].

Table 2
Thermodynamic parameters by MM/GB(PB)SA-based binding free energy (kcal/mol)

Complex	ΔE_{vdW}	ΔE_{elec}	ΔG_{gas}	ΔG_{GB}	ΔG_{SA}	ΔG_{solv}	ΔG_{bind}
INH1	–30.78 ±0.22	–5.89 ± 0.20	–36.66 ±3.1	15.23 ± 0.20	–3.83 ± 0.03	11.39 ± 0.18	–25.27 ± 0.24
INH2	–17.22 ±0.31	–4.05 ± 0.16	–21.27 ±0.41	10.24 ± 0.22	–2.15 ± 0.04	8.08 ± 0.19	–13.19 ±0.27
INH3	–30.84 ± 0.17	–6.69 ± 0.14	–37.54 ± 0.29	16.06 ± 0.17	–3.78 ± 0.019	12.28 ± 0.15	–25.26 ± 0.16
RAL	–39.42 ± 0.14	–21.51 ± 0.27	–60.93 ± 0.30	38.25 ± 0.23	–4.82 ± 0.014	33.42 ± 0.23	–27.50 ± 0.14

Note: ΔG_{bind} represents the gas-phase free energy of binding; ΔE_{ele} and ΔE_{vdw} denote the changes in electrostatic and van der Waals energies, respectively.

The parent group in the INLAIs is based on a benzene scaffold. The inhibitors used in the study contain either the carboxyl and tert-butoxy groups (e.g., BDM-2 and MUT871) or a derivative in which the tert-butoxy side chain is replaced by a cyclopropyloxy group. MUT871 differs from BDM-2 by a methyl substituent on the chromane group, while MUT872 differs from MUT871 by having a second cyclopropyloxy group that replaces the tert-butoxy side chain. Figures 3 and 4 show the interaction diagrams (**a**, **c**, **e**, and **g**) between the interacting residues and INH1, INH2, INH3, and RAL. In the same vein, their respective per-residue energy contribution plots for HIV-1 integrase and the pocket bound to the inhibitors are shown in the same **Figures**. Each complex or system was decomposed into van der Waals, electrostatic, and total energies using the MMGBSA-PRED method. The highest contributing amino acid residues for the INH1, INH2, INH3, and RAL include THR125 (–1.675 kcal/mol), LEU102 (–0.825 kcal/mol), TRP132 (–1.945 kcal/mol), and PRO109 (–2.384 kcal/mol, respectively. Energy contributions by ALA98 in binding to the test inhibitors are significantly similar. In other words, ALA98 contributed values of -0.605 kcal/mol, -0.294 kcal/mol, and -0.992 kcal/mol to binding INH1, INH2, and INH3, respectively.

3.2.2 Per Residue Energy Decomposition (PRED)

The hydrophobic interactions of LEDGF/p75 with amino acid residues include LEU102, ALA128, ALA129, AND TRP132, and a-chain residues THR-174 and MET-178 (Cherepanov, Ambrosio, et al., 2005). Extensive hydrophobic HIV-1 IN catalytic core domain residues LEU102, THR124, THR125, ALA128, ALA129, TRP132, ALA169, GLN168, AND MET178 have also been established for INLAIs (Bonnard et al., 2023). During our findings, the energy contributions of the amino acid residues LEU102 and TRP132 were commonly observed to interact with the INH2, INH3, and RAL systems. The resonating benzene ring substituent on the chromane group of INH1, INH2, and INH3 formed strong hydrophobic interactions, such as Mixed pi/alkyl (alkyl and pi-alkyl), and pi-hydrophobic (pi-pi T-shaped). THR125 formed a non-classical hydrogen bond with INH1. Similarly, GLN95 formed non-classical hydrogen bonds (C–H) with the INH2 chromane group, but THR125 formed conventional hydrogen bonds with the O atom of the INH2 chromane group. In contrast, hydrophobic interactions, including pi-pi stacking, alkyl, and pi-alkyl, were observed between HIV-1 IN and the compound INH3.

Furthermore, TYR99 and TRP132 formed pi-alkyl interactions with benzene and chromane groups, while LEU102 formed a strong alkyl group with the resonating benzene of the parent group. Additional interactions of these inhibitors are stated in Table 3. Therefore, the investigated inhibitors demonstrated a potential mechanism of action against HIV-1 IN integrase, highlighting their promise as possible candidates for disrupting/inhibiting integrase-mediated roles in HIV-1 infection.

Table 3
Interaction residues and the underlying forces of the inhibitor's mechanism of action

Ligand	Interacting amino acids				
	Conventional Hydrogen bond	Carbon hydrogen bond	*Pi-alkyl and* Alkyl	*Pi-pi* stacked	*Pi*-T-Shaped
INH1		THR125	TYR6 TRP15 LYS46 ILE48 ALA98 ALA128 ALA129		
INH2	GLN95	THR125	ALA98 ALA129 TYR99 LEU102 TRP132		
INH3			LYS46 ILE48 ALA98 LEU102 ALA128 ALA129 TYR132	TYR99	
INH4	ALA105 VAL110 LYS111	ALA56 PRO109	MET55 LEU102		TRP132

3.2.3 Analysis of Protein Stability and Flexibility

The structural convergence and stability of the bound and unbound IN CCD-CTD systems were investigated by computing the atomistic C-α backbone RMSD. Lengthy molecular dynamics simulations are crucial because they allow the exploration of a broader range of conformational states of biomolecules, such as proteins and nucleic acids, including infrequent or transient states, which are essential for understanding the stability and function of protein systems [72][73][74]. In contrast, shorter simulations may not capture rare events or reach equilibrium, potentially leading to an incomplete or inaccurate representation of the protein's behaviour [75].

An increased RMSD value for a protein indicates greater atomistic deviation and implies an unstable protein structure, while a decrease in the RMSD value indicates reduced conformational deviation and a highly stable protein[73]. Here, the C-α RMSD values of the unbound and ligand-bound HIV-1 IN CCD-CTD systems were computed and compared to understand the convergence dynamic stability of the systems relative to their initial positions.

As shown in Fig. 5a, the systems converged and remained relatively stable at the beginning of the MD simulation. Table 4 shows the computed average RMSD, RMSF, and RoG values. The deviation (Å) was observed to vary with time, with mean values of 2.27, 2.57, 2.28, 2.23, 2.56, and 2.56 for the Apo, INH1-IN, INH2-IN, INH3-IN, RAL-IN, and RWR-IN systems, respectively. This implies that while INH1 and RWR exhibited a little bit higher motions (or deviations) in the backbone atoms, indicative of their active conformation, an insignificant reduction in the atomistic deviation of INH2, INH3, and INH4 could indicate less INH1-IN structural activity upon ligand-binding. Moreover, the low mean RMSD values imply

that the ligands maintained similar poses at the docked site during simulation, indicative of stable systems [76].

Furthermore, the flexibility of the HIV-1 IN CCD-CTD upon binding to the BDM-2 analogues is compared to the standard drug and unbound system. The dynamics of contributing amino acids form a part of protein building blocks and play a critical role in the overall protein's function [77]. While it might seem counterintuitive, more stable proteins often exhibit greater fluctuations in molecular dynamics (MD) simulations, as shown by INH3-bound IN, due to their inherent flexibility and ability to explore a wider range of conformational states while remaining within their stable folded structure [78]. At the atomic level, these fluctuations do not indicate instability but rather reflect the dynamic nature of HIV-1 IN CCD-CTD and its ability to perform its biological function. These RMSD results were corroborated with findings from C-α RMSF calculations, predictive of flexibility, which revealed insignificantly higher mean values of 1.5 Å, 1.5 Å, and 1.6 Å for INH1-IN, INH2-IN, and INH3, respectively, compared to the unbound and RWR-bound systems, each having 1.4 Å (Fig. 5, Table 4). However, the RAL-bound IN complex exhibited a greater reduction with a mean RMSF value of 1.3 Å, which could imply a slight decrease in structural mobility or flexibility of the IN's atoms over the simulation time.

In addition, Fig. 1b (square boxes) indicates that residues 80–140 and 169–175 exhibited high fluctuations in INH3-bound and RAL-bound HIV-1 IN complexes compared to the unbound HIV-1 IN system. The high fluctuations were caused by interacting residues, including ALA98, LEU102, ALA105, PRO109, ALA129, and TRP132.

Table 4
Showing the mean values and standard error of mean (SEM) for RMSD, RMSF, and ROG data. All values are measured in Angstrom (Å).

System	RMSD	RMSF	ROG
Apo	2.27 ± 0.37	1.40 ± 0.07	19.81 ± 0.19
INH1-IN	2.57 ± 0.52	1.50 ± 0.06	19.87 ± 0.19
INH2-IN	2.28 ± 0.42	1.50 ± 0.06	19.74 ± 0.23
INH3-IN	2.23 ± 0.40	1.60 ± 0.06	19.63 ± 0.19
RAL-IN	2.33 ± 0.40	1.30 ± 0.05	19.42 ± 0.16
RWR	2.56 ± 0.00	1.40 ± 0.64	14.85 ± 0.13

3.2.4 Analysis of Compactness and Mobility of the HIV-1 IN CCD-CTD

To further gain insights into the function and structural conformation of HIV-1 IN CCD-CTD, we measured the compactness of all the protein systems, including the Apo, INH1-bound, MUT871-bound, MUT872-bound, RAL-bound, and RWR-bound systems, to allow comparison and provide useful mobility behaviour

of HIV-1 IN CCD-CTD at the atomistic level. A relation exists between the C-α RoG and the compactness of a protein structure. RoG results can aid critical understanding of the structural and functional activity of a target, helpful in designing a drug against an enzyme. Moreover, the physiological attributes (e.g., closely related to the disease it treats, druggability, and leading to a desirable therapeutic effect) [79]. The loss in the structural compactness of a protein results from the high radius of gyration [80]. Proteins with higher RoG values will be less compact and more mobile, and vice versa. Thus, we computed RoG values and determined the impact of the inhibitors' binding on the compactness and mobility of the HIV-IN CCD-CTD allosteric site.

The mean RoG value of the unbound (Apo) was calculated to be 19.81 ± 0.13 Å, which did not differ significantly from the mean RoG of the systems (Fig. 5D), except for the co-crystal RWR-bound (14.85 ± 0.13 Å), indicating similar compactness and mobility behaviour. Although an ideal situation is that the unbound protein is less compact. Overall, the results showed that ligand binding does not affect conformational changes in HIV-1 IN.

3.2.5 Principal Component Analysis (PCA)

Principal Components (PCs) are collective motions that describe how atoms move together. This is crucial for understanding how proteins function, as many functional motions involve coordinated movements of multiple residues [81]. PCA transforms the complex atomic motions from the MD simulation into a set of orthogonal vectors (PCs) that represent the principal directions of protein motion. Therefore, visual and clustering analyses of the PCA were performed to transform the 3D coordinates from the frames in the trajectory files of the Apo HIV-1 IN, INH1-bound, INH2-bound, INH3-bound, and RAL-bound systems into a set of linear, orthogonal vectors, or PCs. PCA was performed on the HIV-IN C-α backbone atoms using the CPPTRAJ in AMBER18 GPU to compute the two components, PC1 and PC2. Graphically shown in Fig. 5c, the PC1 (x-axis) and PC2 (y-axis) represent a covariance matrix after eliminating eigenvectors. Each PC is associated with an eigenvalue and eigenvector, indicating the amount of variance (or fluctuation) explained by that PC. The larger the eigenvalue, the more significant the motion along that PC. Using the covariance matrix obtained from the averaged structure in Cartesian coordinates to assess convergence in a 200 ns MD simulation, we determine the modes of motion and compare positional fluctuations in the dynamically simulated structures. The scatter plot shows the unbound HIV-IN (black), INH1-IN (red), INH2-IN (green), INH3-IN (blue), and RAL-IN (cyan). A distinct motion separation was observed in the five systems. However, a more correlated structure was observed in the INH3-bound state along the two principal components, PC1 and PC2, compared to the apo and other ligand-bound systems.

The PCA plot shows that the conformations converge in conformational space. Every dot describes one atom's x and y coordinates for every step in each respective system trajectory file. While cluster contractions were prominent in the INH3-bound and RAL-bound complexes, the potential inhibitor-bound system showed cluster growth, indicating significant conformational shifts across the systems. Moreover, multiple clusters were observed in all systems, especially in the INH3- and RAL-bound complexes, indicating metastability or the presence of numerous conformational states that spend long

periods in distinct local states. Therefore, this finding may imply conformational changes (or dynamic events) in the HIV-IN CCD-CTD protein.

3.2.6 Defined Secondary Structure (DSSP) Protein Analysis

To gain more insights into the structural conformation and binding mechanisms that can lead to the potential inhibition of BDM-2, MUT871, and MUT872 compared to RAL, we investigated the secondary structure elements of the HIV-1 IN CCD-CTD protein. DSSP assigns secondary structure elements based on hydrogen bonding patterns and geometric criteria. Common assignments include a*lpha-helix*, *beta-bridge*, *extended strand* (*beta-sheet*), 3-helix (3_{10} *helix*), *5-helix* (*pi-helix*), *turn*, *bend*, and c*oil* [64]. As shown in the legend of Fig. 6, integers (from 0 to 7) indicate *None*, *Para*, *Anti*, 3_{10}, *Alpha*, *Pi*, *Turn*, and *Bend*, respectively. The conversion into *turn*, *bend*, and *pi-helix* structures suggests a potential reduction in hydrogen bonds compared with transitions into *beta sheets*, *alpha helices*, and 3_{10} *helices* [30]. The DSSP plots of the unbound and ligand-bound systems displayed some significant similarities and differences in their secondary structures.

The plots showed that transitions occurred around residues 36–40, from the bend to the turn, and 51–54, from the helix to the turn, especially in the INH1-, INH2-, and INH3-bound states. Various noticeable changes, such as twisting and coiling, are seen to characterise residues 7–20, 24–28, 49–56, and 177–185.

In addition, there are significant changes (unwinding) in the strand and helix that occur over time, while little or no change occurs in the other region, including the active site, N-terminal, and catalytic core domains, which may influence the functional roles of zinc binding and catalysis in HIV IN, respectively.

Moreover, Figs. 7(**a and b**) show visual structural changes in the conformations of the superimposed bound and unbound systems, corroborating the DSSP plots, and providing deeper insights into the inter-residual displacements. The larger segments of the secondary structure conformations remain stable throughout the MD simulations, while the region cycled in Figures a and b show fluctuations. Overall, the complexes show little fluctuation in the secondary structures, indicating stability.

3.2.7. Distance Matrix Analysis

Distance (*D*, Å) matrix analysis of molecular dynamics (MD) simulations is a powerful technique for understanding protein structure and dynamics. A distance matrix is generated by calculating the distances between all pairs of atoms (or residues) at each time step of an MD simulation. The distance parameter can be used to visualise conformational changes, identify correlated motions, and quantify structural differences between protein states. Figure 8 shows the distances measured by ALA98 and TRP132, as well as the distance between LEU102 and TRP132. For clarity, the measured distances are given in Table 5. These binding-pocket residues were chosen because they showed strong binding forces and high energy contributions to inhibitor binding in this study, as seen in the interaction diagrams and PRED, respectively. For each system, the snapshots were obtained at various time (ns) scales, including

1, 10, 50, 100, 200, and 300. Distances (Å) were computed between the residues in the unbound protein and compared to the distances in the bound complexes.

For instance, the distance (*D1*) between ALA98 and TRP132 decreases specifically and significantly at various time points up to 50 ns, then increases slightly and gradually at 100 and 200 ns, and finally decreases after 310 ns. Although there was a significant decrease from 10.25 to 8.86, the final distance between ALA98 and TRP132 was 9.97 Å, while there were no considerable distance changes in the distance (*D2*) between LEU102 and TRP132. In contrast, the distance (*D1*) of the INH-bound systems, except INH2-bound IN, decreases and increases, but gives final distance values (at 310 ns) significantly lower than the respective distance values at zero ns. Whereas the distances (*D1*) INH2-bound IN increased throughout the simulation time, *D2* consistently increased and decreased. Therefore, characteristic conformations reveal that the protein adopts open and closed conformations for all the systems, especially for ligand-bound complexes. Differences were observed among amino acid residues in the unbound protein and the ligand-bound systems, and the distance variations might be due to the ligand's bulky structure. Moreover, the distance unfolds the non-covalent interactions in this study, including the conventional and non-classical hydrogen bonds and hydrophobic contacts. The optimal distances (*D1* and *D2*) throughout the trajectory reveal very insightful information.

Figure 9(a-e) shows the superimposed structures of the unbound and ligand-bound HIV-1 CCD-CTD complexes during 310 ns MD simulations. The visual images revealed slight differences across the systems; 1 ns (yellow), 2 ns (green), 5 ns (blue), 10 ns (orange), 15 ns (magenta), 20 ns (purple), 25 ns (forest green), 50 ns (deep sky blue), 100 ns (brown), 150 ns (acquamarine), 200 ns (tan), 250 ns (dark cyan), 300 ns (khaki), 310 ns (gray).

Table 5
The distances, *d* (Å), between amino acid (*D1*) Trp132-Leu102 (*D2*) Trp132-Ala98

Time (ns)	Distances	APO	INH1-IN	INH2-IN	INH3-IN	RAL-IN
0	D1	10.25	10.99	7.99	9.06	9.43
	D2	10.99	11.50	11.78	11.82	12.98
10	D1	9.31	8.88	9.73	10.20	10.76
	D2	10.96	10.80	10.01	12.36	13.88
50	D1	8.86	9.27	7.86	11.36	9.06
	D2	10.90	13.19	13.05	12.41	13.54
100	D1	9.21	9.88	9.20	9.88	10.38
	D2	10.72	12.73	13.39	11.09	11.10
200	D1	10.64	8.26	8.25	7.68	9.39
	D2	10.46	12.99	12.61	12.32	12.59
300	D1	9.97	10.34	10.34	7.65	8.73
	D2	11.49	11.66	11.66	11.79	11.93

CONCLUSION

The design of small-molecule compounds as strand transfer inhibitors (INSTIs) and the highlight of the IN allosteric inhibitor (INLAIs) strategy exemplify targeted HIV therapy. Recently, this therapeutic strategy led to the discovery of new INLAI chromane-functionalised compounds, including BDM-2 (INH1), MUT871 (INH2), and MUT872 (INH3), which are potent allosteric inhibitors. The compounds specifically target the HIV-1 integrase CCD-CTD interface by mimicking the LEDGF/p75 binding motif. MUT871 (IC50 = 14 nM) acts as a “molecular glue”, inducing premature and aberrant hyper-multimerisation of the IN protein. Thus, the mechanism disrupts the normal IN-LEDGF/p75 interaction, preventing proper HIV-1 particle maturation and viral integration, thereby inhibiting replication. Hence, it was necessary to investigate the motion and dynamics of the protein structure and its conformations, and to depict the activities of these allosteric inhibitors, along with the mechanisms by which they inhibit particle maturation and viral integration at the atomic level. Therefore, this study provides a comprehensive analysis of the motion and dynamics of the structure and functions of the HIV-1 integrase CCD-CTD domains, and the mechanism of inhibition by potential HIV-IN subtype B allosteric inhibitors upon binding to the HIV-1 integrase CCD-CTD interface. Using the combination of molecular docking, binding energy calculations, and molecular dynamics simulations, the post-MD simulation snapshots of the bound and unbound HIV-1 IN systems exhibited characteristic structural behaviour, particularly at the binding pocket and the proximal residues of the secondary structures. Structural transition and twisting

were observed at different simulation times. In addition, the residues within and proximal to the active site showed little fluctuation in the larger regions and high fluctuations around the binding site. Thus, the compounds BDM-2, MUT871, and MUT872 showed promising potency. The MM/PBSA binding free energy estimations revealed that BDM-2 and MUT872 were bound to the HIV-1 IN CCD-CTD interface with considerably high affinities, as evidenced from the relatively high ΔG values compared to INH2. Additionally, molecular visualisation showed that INH1 and INH3 were buried within the CCD pocket. These findings unravel a model that describes the motion and dynamic conformational changes at the HIV-1 CCD-CTD interface upon ligand binding, and also elaborate on the mechanism by which the BDM-2 compound derivatives inhibit HIV-1, which could further enhance the design of effective and potent targeted antiviral therapy.

Declarations

Author Contributions

Conceptualisation: A.T.A., and S.M.

Methodology: A.T.A, and S.M.,

Software: A.T.A. and S.M.

Validation: A.T.A, S.T.L., and S.M.

Formal Analysis: A.T.A, S. T. L, and S. M.

Writing (original draft): A.T.A.

Writing (review): A.T.A., S. T. L., and S.M.

Supervision: S.M.

All authors have read and agreed to the published version of the manuscript.

Funding: The research received no external funding.

Data Availability Statement: Data will be made available on request.

Disclosure statement: The authors declare no potential conflict of interest.

Acknowledgement

First, the authors acknowledge the ALMIGHTY GOD who created all things, including life, wisdom, and knowledge for every human being. We thank the Centre for High-Performance Computing (CHPC, www.chpc.ac.za) for providing computational resources. Lastly, the authors appreciate the Department

of Life and Consumer Sciences and the University of South Africa at large for providing funding for this postdoctoral fellowship and for their other support.

References

1. United Nations on HIV/AIDS, Global (2024) FACT SHEET HIV statistics People living with HIV People living with HIV accessing antiretroviral therapy New HIV infections AIDS-related deaths People most affected by HIV, 2024. [Online]. Available: https://www.unaids.org/en/resources/fact-sheet
2. Carter A et al (2024) Global, regional, and national burden of HIV/AIDS, 1990–2021, and forecasts to 2050, for 204 countries and territories: the Global Burden of Disease Study 2021. Lancet HIV 11(12):e807–e822. 10.1016/S2352-3018(24)00212-1
3. Mody A, Sohn AH, Iwuji C, Tan RKJ, Venter F, Geng EH (2024) HIV epidemiology, prevention, treatment, and implementation strategies for public health. Lancet 403(10425):471–492. 10.1016/S0140-6736(23)01381-8
4. Gedefie A et al (2024) Prevalence and determinants of HIV among reproductive-age women (15–49 years) in Africa from 2010 to 2019: a multilevel analysis of demographic and health survey data. Front Public Heal 12:1–11. 10.3389/fpubh.2024.1376235
5. Mabaso M, Makola L, Naidoo I, Mlangeni LL, Jooste S, Simbayi L (2019) HIV prevalence in South Africa through gender and racial lenses: results from the 2012 population-based national household survey. Int J Equity Health 18(167):1–11
6. Amee S, Stephen McCracken SS, Frederix K, Tierney R, Koto M, Ahmed N, Thin K, Dobbs T, Mosilinyane AL, Letsie B, Parekh H, Patel S, Birhanu L, Wiesner (2022) High HIV prevalence and associated factors in Lesotho: Results from a population-based survey. PLoS ONE 17(7):e0271431. 10.1371/journal.pone.0271431
7. Mnyaka OR, Mabunda SA, Chitha WW, Nomatshila SC, Ntlongweni X (2021) Barriers to the Implementation of the HIV Universal Test and Treat Strategy in Selected Primary Care Facilities in South Africa ' s Eastern Cape Province. J Prim Care Community Health 12:1–12. 10.1177/21501327211028706
8. Kim H, Tanser F, Tomita A, Vandormael A, Cuadros DF (2021) Beyond HIV prevalence: Identifying people living with HIV within underserved areas in South Africa. BMJ Glob Heal 6:1–10. no. e00408910.1136/bmjgh-2020-004089
9. Sankarananthan M (2019) HIV - Is a cure possible? Indian J Sex Transm Dis AIDS 40(1):1–5. 10.4103/ijstd.IJSTD_112_15
10. Foka FET, Mufhandu HT (2023) Current ARTs, Virologic Failure, and Implications for AIDS Management: A Systematic Review. Viruses 15(1732):1–28. 10.3390/v15081732
11. Koren DE, Chahine EB, Sherman EM (2025) Lenacapavir: A Twice-Yearly Injectable for HIV Preexposure Prophylaxis. Ann Pharmacother 60(3):276–286. 10.1177/10600280251379877

12. Margot NA et al (2022) Resistance Analyses in Highly Treatment-Experienced People with Human Immunodeficiency Virus (HIV) Treated with the Novel Capsid HIV Inhibitor Lenacapavir. J Infect Dis 226(11):1985–1991. 10.1093/infdis/jiac364
13. Wirden M et al (2024) Ultra-rapid selection of the N74D capsid inhibitor resistance mutation after 3weeks on lenacapavir. J Antimicrob Chemother 79(7):1706–1707. 10.1093/jac/dkae115
14. Esposito D, Craigie R (1999) HIV integrase structure and function. Adv Virus Res 52:319–333. 10.1016/s0065-3527(08)60304-8
15. Li Y, Xuan S, Feng Y, Yan A (2015) Targeting HIV-1 integrase with strand transfer inhibitors. Drug Discov Today 20(4):435–449. 10.1016/j.drudis.2014.12.001
16. Lesbats P, Engelman AN, Cherepanov P (2016) Retroviral DNA Integration. Chem Rev 116(20):12730–12757. 10.1021/acs.chemrev.6b00125
17. Davies DR (2004) Structure and Function of HIV-1 Integrase. Curr Top Med Chem 4(9):965–977. https://doi.org/10.2174/1568026043388547
18. Smith SJ, Zhao XZ, Passos DO, Lyumkis D, Burke TR, Hughes SH (2021) Integrase Strand Transfer Inhibitors Are Effective Anti-HIV Drugs. Viruses 13(205):1–28. https://doi.org/10.3390/v13020205
19. Ilona K, Jóźwik D, Passos, Lyumkis D (2020) Structural biology of HIV integrase strand transfer inhibitors. Trends Pharmacol Sci 41(9):611–626. 10.1016/j.tips.2020.06.003
20. Mbhele N, Chimukangara B, Gordon M (2021) HIV-1 integrase strand transfer inhibitors: a review of current drugs, recent advances and drug resistance. Int J Antimicrob Agents 57(5):106343. 10.1016/j.ijantimicag.2021.106343
21. Bonnard D et al (2023) Biological and Structural Analyses of New Potent Allosteric Inhibitors of HIV-1 Integrase. Antimicrob Agents Chemother 67(7). 10.1128/aac.00462-23
22. Ndashimye E, Reyes PS, Arts EJ (2023) New antiretroviral inhibitors and HIV-1 drug resistance: more focus on 90% HIV-1 isolates? FEMS Microbiol Rev 47(1):1–22. 10.1093/femsre/fuac040
23. Cherepanov P, Ambrosio ALB, Rahman S, Ellenberger T, Engelman A (2005) Structural basis for the recognition between HIV-1 integrase and transcriptional coactivator p75, *Proc. Natl. Acad. Sci. U. S. A.*, vol. 102, no. 48, pp. 17308–17313. 10.1073/pnas.0506924102
24. Cherepanov P, Sun ZYJ, Rahman S, Maertens G, Wagner G, Engelman A (2005) Solution structure of the HIV-1 integrase-binding domain in LEDGF/p75. Nat Struct Mol Biol 12(6):526–532. 10.1038/nsmb937
25. Vansant G et al (2020) The chromatin landscape at the HIV-1 provirus integration site determines viral expression. Nucleic Acids Res 48:7801–7817. 10.1093/nar/gkaa536
26. Engelman A, Kessl JJ, Kvaratskhelia M (2013) Allosteric inhibition of HIV-1 integrase activity. Curr Opin Chem Biol 17(3):339–345. 10.1016/j.cbpa.2013.04.010
27. Patel D et al (2016) A new class of allosteric HIV-1 integrase inhibitors identified by crystallographic fragment screening of the catalytic core domain. J Biol Chem 291(45):23569–23577. 10.1074/jbc.M116.753384

28. Dinh LP et al (2022) Multi-Substituted Quinolines as HIV-1 Integrase Allosteric Inhibitors. Viruses 14(1466):1–13. 10.3390/v14071466
29. Bonnard D et al (2018) Structure-function analyses unravel distinct effects of allosteric inhibitors of HIV-1 integrase on viral maturation and integration. J Biol Chem 293(16):6172–6186. 10.1074/jbc.M117.816793
30. Al-Mohaya M, Mesut B, Kurt A, Çelik YS (2024) In silico approaches which are used in pharmacy. J Appl Pharm Sci 14(4):225–239. 10.7324/JAPS.2024.154854
31. Pettersen EF et al (2004) UCSF Chimera — A Visualization System for Exploratory Research and Analysis. J Comput Chem 25(13):1605–1612. 10.1002/jcc.20084
32. Krenn WM, Oluyemi BB, Samuel AT, Adewumi YA, Adekunle MES, Soliman L (2022) An Allosteric Inhibitory Potential of Triterpenes from Combretum racemosum on the Structural and Functional Dynamics of Plasmodium falciparum Lactate Dehydrogenase Binding Landscape, *Chem. Biodivers.*, vol. 19, no. e202100646, pp. 1–20. 10.1002/cbdv.202100646
33. Eberhardt J, Santos-Martins D, Tillack AF, Forli S, AutoDock Vina 1.2.0: New Docking Methods, Expanded Force Field, and, Bindings P (2021) *J. Chem. Inf. Model.*, vol. 61, no. 8, pp. 3891–3898. 10.1021/acs.jcim.1c00203
34. Trott O, Olson AJ (2010) AutoDock Vina: Improving the speed and accuracy of docking with a new scoring function, efficient optimization, and multithreading. J Comput Chem 31(2):455–461. 10.1002/jcc.21334
35. Meng M, Zhang XY, Mezei HX M., and, Cui (2011) Molecular Docking: A powerful approach for structure-based drug drug discovery. Curr Comput Aided Drug Des 7(2):146–157. 10.2174/157340911795677602
36. Adewumi AT, Soremekun OS, Ajadi MB, Soliman MES (2020) Thompson loop: Opportunities for antitubercular drug design by targeting the weak spot in demethylmenaquinone methyltransferase protein. RSC Adv 10(39):23466–23483. 10.1039/d0ra03206a
37. Moonsamy S, Bhakat S, Ramesh M, Soliman MES (2017) Identification of Binding Mode and Prospective Structural Features of Novel Nef Protein Inhibitors as Potential Anti-HIV Drugs. Cell Biochem Biophys 75(1):49–64. 10.1007/s12013-016-0774-1
38. Deng N et al (2016) Allosteric HIV-1 integrase inhibitors promote aberrant protein multimerization by directly mediating inter-subunit interactions: Structural and thermodynamic modeling studies. Protein Sci 25(11):1911–1917. 10.1002/pro.2997
39. Lang S (2025) Understanding the HIV-CA protein and the ligands that bind at the N-terminal domain (NTD) - C-terminal domain (CTD) interface. RSC Med Chem 16(6):2373–2387. 10.1039/d5md00111k
40. Adewumi AT, Mosebi S (Dec. 2023) Characteristic Binding Landscape of Estrogen Receptor-α36 Protein Enhances Promising Cancer Drug Design. Biomolecules 13(12):1798. 10.3390/biom13121798

41. Mortier J, Rakers C, Bermudez M, Murgueitio MS, Riniker S, Wolber G (2015) The impact of molecular dynamics on drug design: Applications for the characterization of ligand-macromolecule complexes. Drug Discov Today 20(6):686–702. 10.1016/j.drudis.2015.01.003
42. Şterbuleac D (2021) Molecular dynamics: A powerful tool for studying the medicinal chemistry of ion channel modulators. RSC Med Chem 12(9):1503–1518. 10.1039/d1md00140j
43. Zhang HL et al (2023) Analysis of aptamer-target binding and molecular mechanisms by thermofluorimetric analysis and molecular dynamics simulation. Front Chem 11:1–12. 10.3389/fchem.2023.1144347
44. Adewumi AT et al (2023) Propitious Indazole Compounds as β-ketoacyl-ACP Synthase Inhibitors and Mechanisms Unfolded for TB Cure: Integrated Rational Design and MD Simulations, *ChemistrySelect*, vol. 8, no. e202203877, pp. 1–18, 10.1002/slct.202203877
45. Case DA et al (2007) The Amber Biomolecular Simulation Programs. J Comput Chem 26(16):1668–1688
46. Lee TS et al (2018) GPU-Accelerated Molecular Dynamics and Free Energy Methods in Amber18: Performance Enhancements and New Features. J Chem Inf Model 58(10):2043–2050. 10.1021/acs.jcim.8b00462
47. Soremekun OS, Olotu FA, Agoni C, Soliman MES (2019) Recruiting monomer for dimer formation: resolving the antagonistic mechanisms of novel immune check point inhibitors against Programmed Death Ligand-1 in cancer immunotherapy. Mol Simul 45(10):777–789. 10.1080/08927022.2019.1593977
48. Wang J, Wolf RM, Caldwell JW, Kollman PA, Case DA (2005) Development and testing of a general amber force field (Journal of Computational Chemistry (2004) 25 (1157)). J Comput Chem 26(1). 10.1002/jcc.20145
49. Case DA et al (2023) AmberTools. J Chem Inf Model 63(20):6183–6191. 10.1021/acs.jcim.3c01153
50. Mark P, Nilsson L (2001) Structure and dynamics of the TIP3P, SPC, and SPC/E water models at 298 K. J Phys Chem A 105(43):9954–9960. 10.1021/jp003020w
51. Onufriev AV, Izadi S (2018) Water models for biomolecular simulations. Wiley Interdiscip Rev Comput Mol Sci 8(2):e1347. 10.1002/wcms.1347
52. Linse JB, Hub JS (2021) Three- And four-site models for heavy water: SPC/E-HW, TIP3P-HW, and TIP4P/2005-HW. J Chem Phys 154(19). 10.1063/5.0050841
53. Kehinde IO, Oduro-Kwateng E, Soliman MES (2024) Allosteric covalent inhibition of TOE1 as potential unexplored anti-cancer target: structure-based virtual screening and covalent molecular dynamics analysis. J Recept Signal Transduct 44(3):97–106. 10.1080/10799893.2024.2411690
54. Ryckaert JP, Ciccotti G, Berendsen HJC (1977) Numerical integration of the cartesian equations of motion of a system with constraints: molecular dynamics of n-alkanes. J Comput Phys 23(3):327–341. 10.1016/0021-9991(77)90098-5
55. Oluwafemi KA et al (2026) Harunganol-B and beyond: unveiling nature ' s arsenal against drug-resistant Acinetobacter baumannii. Silico Pharmacol 14(56):1–18. https://doi.org/10.1007/s40203-

026-00558-y

56. Berendsen HJC, Postma JPM, Van Gunsteren WF, Dinola A, Haak JR (1984) Molecular dynamics with coupling to an external bath. J Chem Phys 81(8):3684–3690. 10.1063/1.448118
57. Gupta S, Senapati S (2019) Mechanism of inhibition of drug-resistant HIV-1 protease clinical isolates by TMC310911: A molecular dynamics study. J Mol Struct 1198:126893. 10.1016/j.molstruc.2019.126893
58. Adewumi AT et al (2023) Probing into the Flap-dimer Dynamics of the Mycobacterium tuberculosis Kasa Enzyme Binding Landscape Provides the Underlying Inhibitory Mechanisms of JSF-3285 and 5G. Curr Top Med Chem 23(12):1065–1080. 10.2174/1568026623666230125124433
59. Seifert E (2014) OriginPro 9.1: Scientific data analysis and graphing software - Software review. J Chem Inf Model 54(5):1552. 10.1021/ci500161d
60. Sargsyan K, Grauffel C, Lim C (2017) How Molecular Size Impacts RMSD Applications in Molecular Dynamics Simulations. J Chem Theory Comput 13(4):1518–1524. 10.1021/acs.jctc.7b00028
61. Soremekun OS, Omolabi KF, Adewumi AT (2020) Exploring the effect of ritonavir and TMC-310911 on SARS-CoV-2 and SARS-CoV main proteases: potential from a molecular perspective. Futur Sci OA 7(1):1–10
62. Genheden S, Ryde U (2015) The MM/PBSA and MM/GBSA methods to estimate ligand-binding affinities. Expert Opin Drug Discov 10(5):449–461. 10.1517/17460441.2015.1032936
63. Adewumi AT, Ramharack P, Soremekun OS, Soliman MES (2020) Delving into the Characteristic Features of ' Menace ' Mycobacterium tuberculosis Homologs: A Structural Dynamics and Proteomics Perspectives. Protein J 39(2):118–132. 10.1007/s10930-020-09890-4
64. Adewumi AT, Elrashedy A, Soremekun OS, Ajadi MB, Soliman MES (2022) Weak spots inhibition in the Mycobacterium tuberculosis antigen 85C target for antitubercular drug design through selective irreversible covalent inhibitor-SER124. J Biomol Struct Dyn 40(7):2934–2954. 10.1080/07391102.2020.1844061
65. Justino GC, Nascimento CP, Justino MC (2021) Molecular dynamics simulations and analysis for bioinformatics undergraduate students. Biochem Mol Biol Educ 49(4):570–582. 10.1002/bmb.21512
66. Adewumi AT et al (2023) Probing into the Flap-dimer Dynamics of the Mycobacterium tuberculosis Kasa Enzyme Binding Landscape Provides the Underlying Inhibitory Mechanisms of JSF-3285 and 5G, *Curr. Top. Med. Chem.*, vol. 23, no. 12, pp. 1065–1080, Jan. 10.2174/1568026623666230125124433
67. Clavel F, HIV RESISTANCE TO RALTEGRAVIR (2009), *Eur J Med Res*, vol. 14, no. Suppl. III, pp. 47–54
68. Malet I et al (2014) New raltegravir resistance pathways induce broad cross-resistance to all currently used integrase inhibitors. J Antimicrob Chemother 69(8):2118–2122. 10.1093/jac/dku095
69. Patel P, Louie S (2018) *Drug Interactions in HIV: Protease and Integrase Inhibitors*. 10.1007/978-3-319-72416-4_7

70. Kiser JJ et al (2010) Effect of antacids on the pharmacokinetics of raltegravir in human immunodeficiency virus-seronegative volunteers. Antimicrob Agents Chemother 54(12):4999–5003. 10.1128/AAC.00636-10
71. Roberts JL, Kiser JJ, Hindman JT, Meditz AL (2011) Virologic failure with a raltegravir-containing antiretroviral regimen and concomitant calcium administration. Pharmacotherapy 31(10):1042. 10.1592/phco.31.10.1042
72. Chandra I, Nayak C, Singh SK (2021) *Predicting Protein Folding and Protein Stability by Molecular Dynamics Simulations for Computational Drug Discovery*. 10.1007/978-981-15-8936-2_7
73. Sultana T, Mou SI, Chatterjee D, Faruk MO, Hosen MI (2024) Computational exploration of SLC14A1 genetic variants through structure modeling, protein-ligand docking, and molecular dynamics simulation. Biochem Biophys Rep 38:101703. 10.1016/j.bbrep.2024.101703
74. Ghosh D, Biswas A, Radhakrishna M (2024) Advanced computational approaches to understand protein aggregation. Biophys Rev 5:1–40. 10.1063/5.0180691
75. Prašnikar E, Ljubič M, Perdih A, Borišek J (2024) Machine learning heralding a new development phase in molecular dynamics simulations Independent Markov decomposition. Artif Intell Rev 57(4):1–36. 10.1007/s10462-024-10731-4
76. Agbebi EA et al (2025) Uvarinol and Dichamanetin Derived from Uvaria chamae as Potential Dual-Site Inhibitors Against PBP2a in Methicillin Resistant Staphylococcus aureus: An In Silico Study, *Pharmaceuticals*, vol. 18, no. 4, Apr. 10.3390/ph18040529
77. Morris R, Black KA, Stollar EJ (2022) Uncovering protein function: from classification to complexes. Essays Biochem 66:255–285. https://doi.org/10.1042/EBC20200108
78. Parray ZA, Shahid M, Islam A (2022) Insights into Fluctuations of Structure of Proteins: Significance of Intermediary States in Regulating Biological Functions. Polym (Basel) 14(8):1–18. 10.3390/polym14081539
79. Singh N, Vayer P, Tanwar S, Poyet JL, Tsaioun K, Villoutreix BO (2023) Drug discovery and development: introduction to the general public and patient groups. Front Drug Discov 3:1–11. 10.3389/fddsv.2023.1201419
80. Lobanov MY, Bogatyreva NS, Galzitskaya OV (2008) Radius of gyration as an indicator of protein structure compactness. Mol Biol 42(4):701–706. 10.1134/S0026893308040195
81. Tan Y, Hanson JA, Chu J, Yang H (2014) *Principal Component Analysis: A Method for Determining the Essential Dynamics of Proteins*, vol. 1084. 10.1007/978-1-62703-658-0

Figures

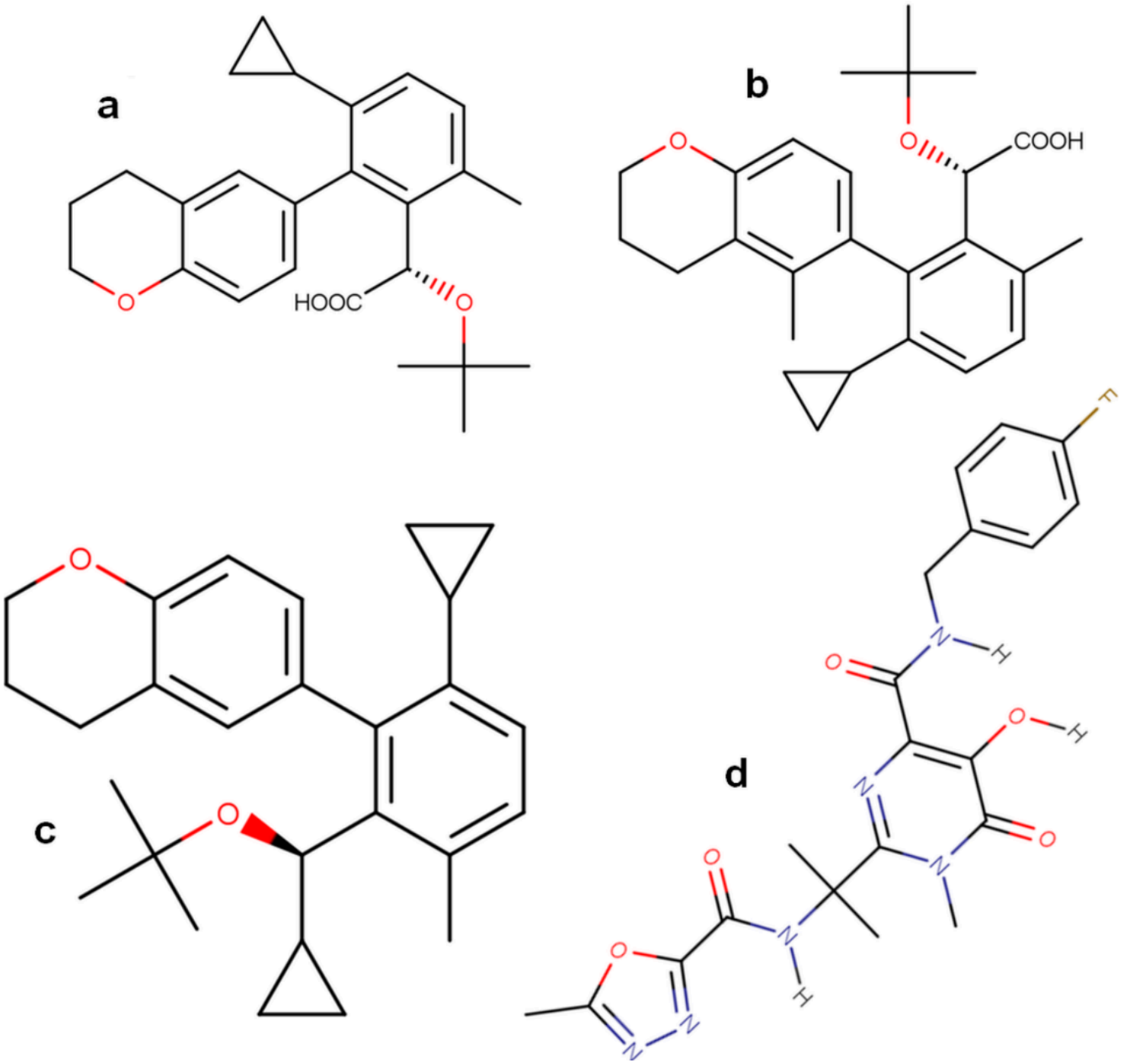


Figure 1

Chemical structures of the study inhibitors of HIV-1 IN CCD-CTD function. INH1 (a), INH2 (b), INH3 (c), and RAL (d).

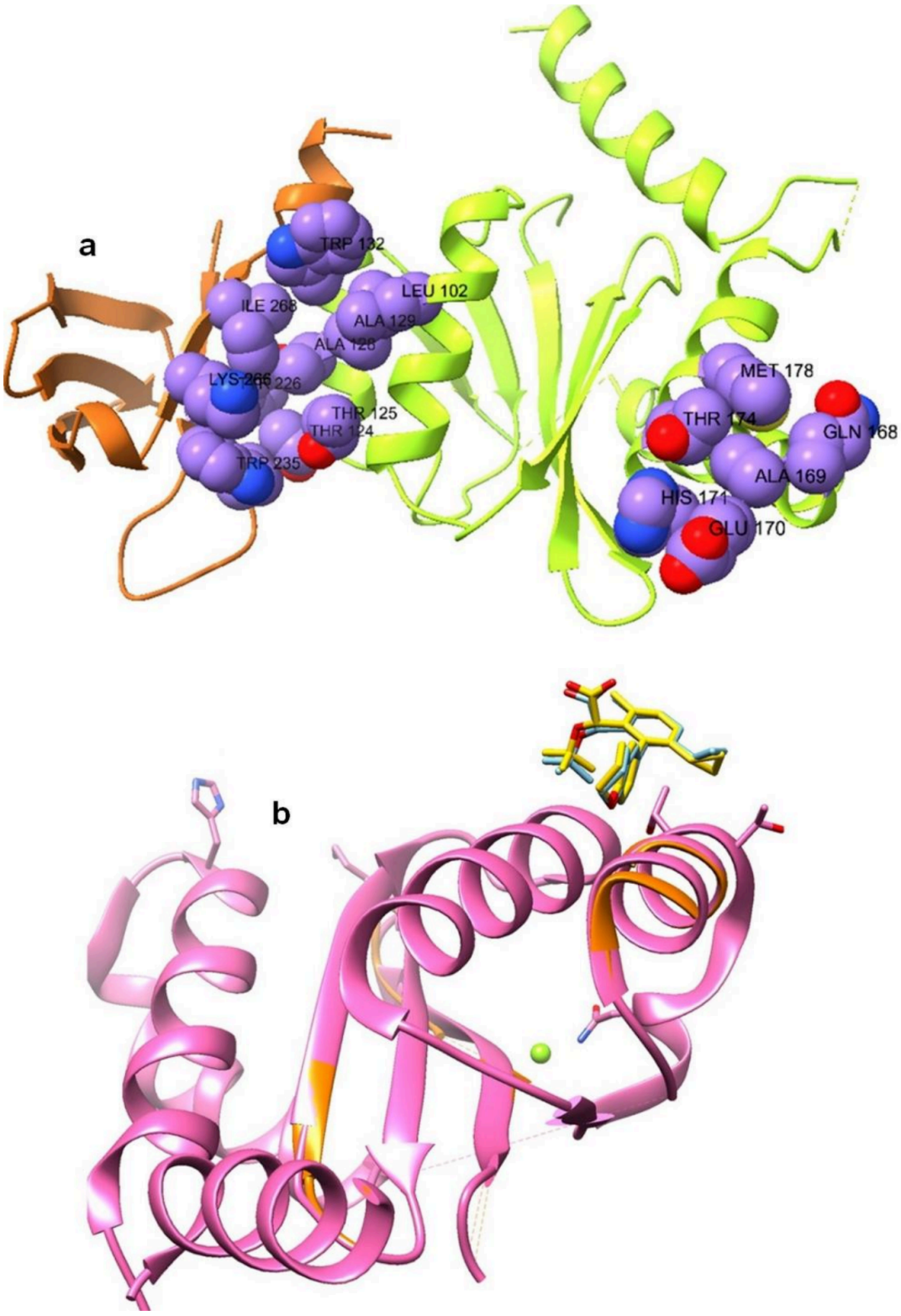


Figure 2

(**a**) HIV-1 IN CCD-CTD active pocket, showing the residues (blue). CCD (yellow-green), CTD (brown colour). (b) Superimposed redocked and experimental co-crystal ligand (RWR) for the validation of the docking protocol by testing the docking parameters.

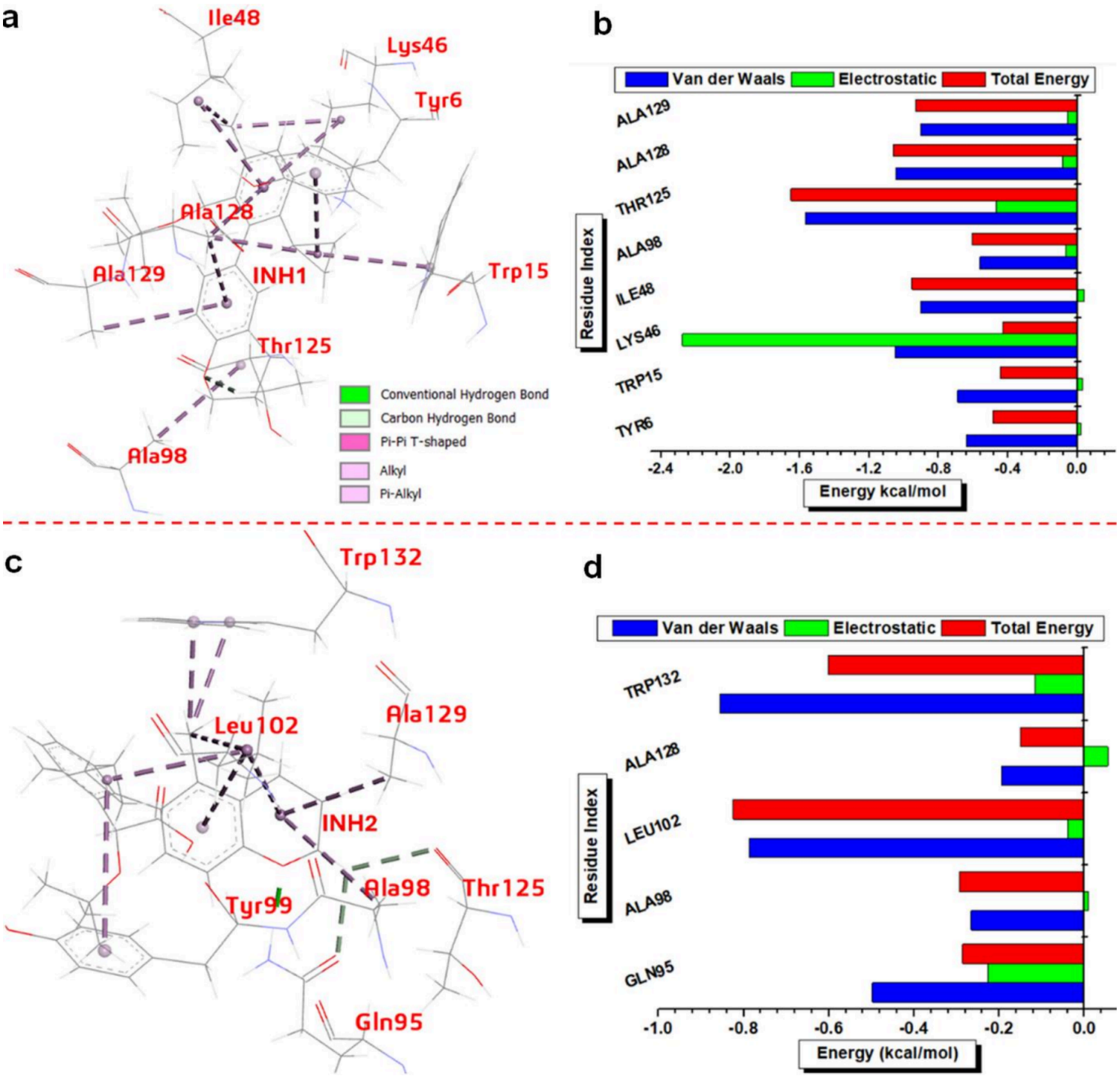


Figure 3

Visual interaction networks. HIV-1 IN-INH1 (a) and HIV-1 IN-INH2 (c). Integrase (IN) CCD-CTD per-residue energy contributions to INH1 (b) and INH2 (d), respectively.

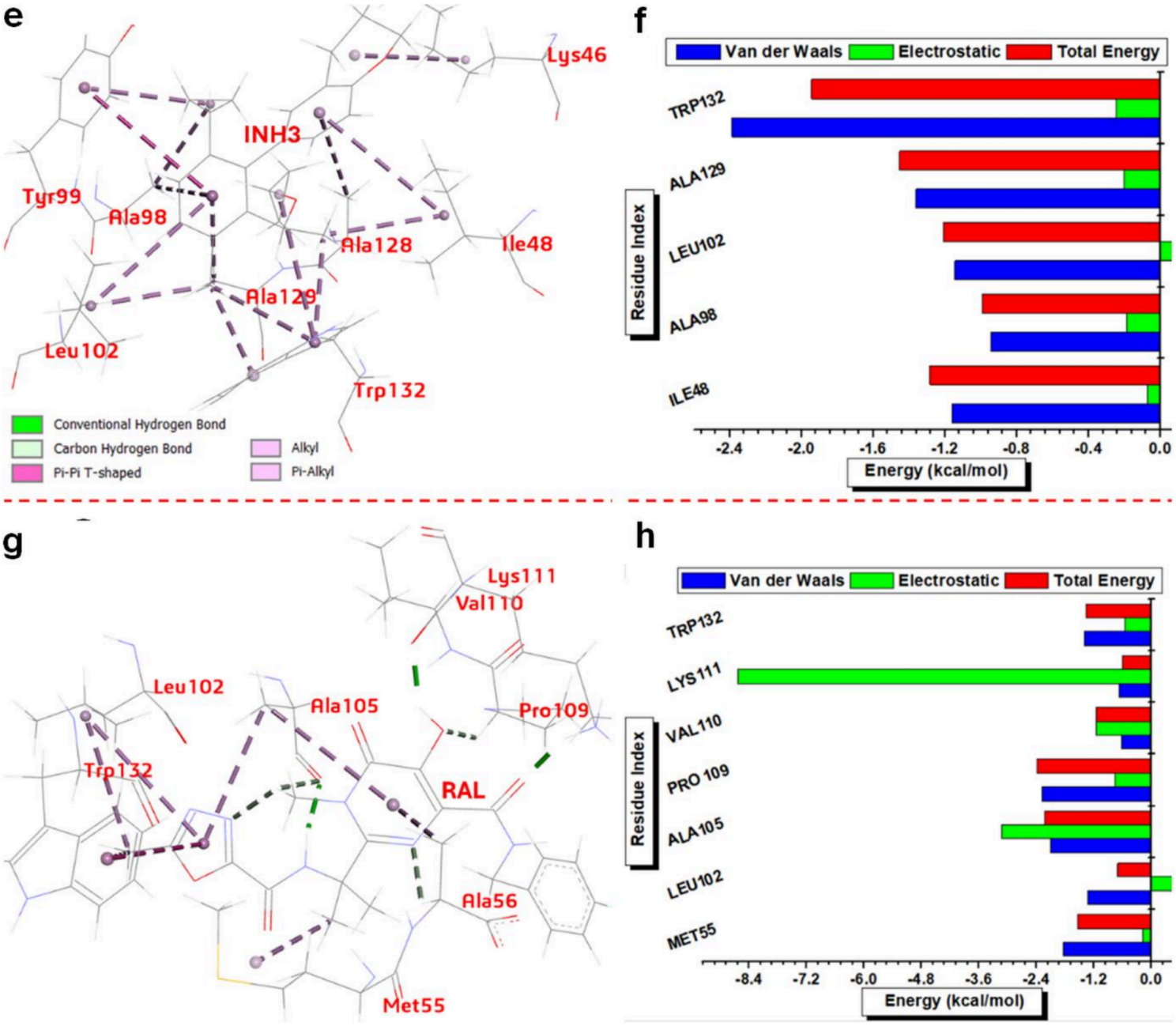


Figure 4

Visual interaction networks. HIV-1 IN-INH3 (e) and HIV-1 IN-INH4 (g). IN CCD-CTD per-residue energy contributions to INH3 (f) and INH4 (h), respectively.

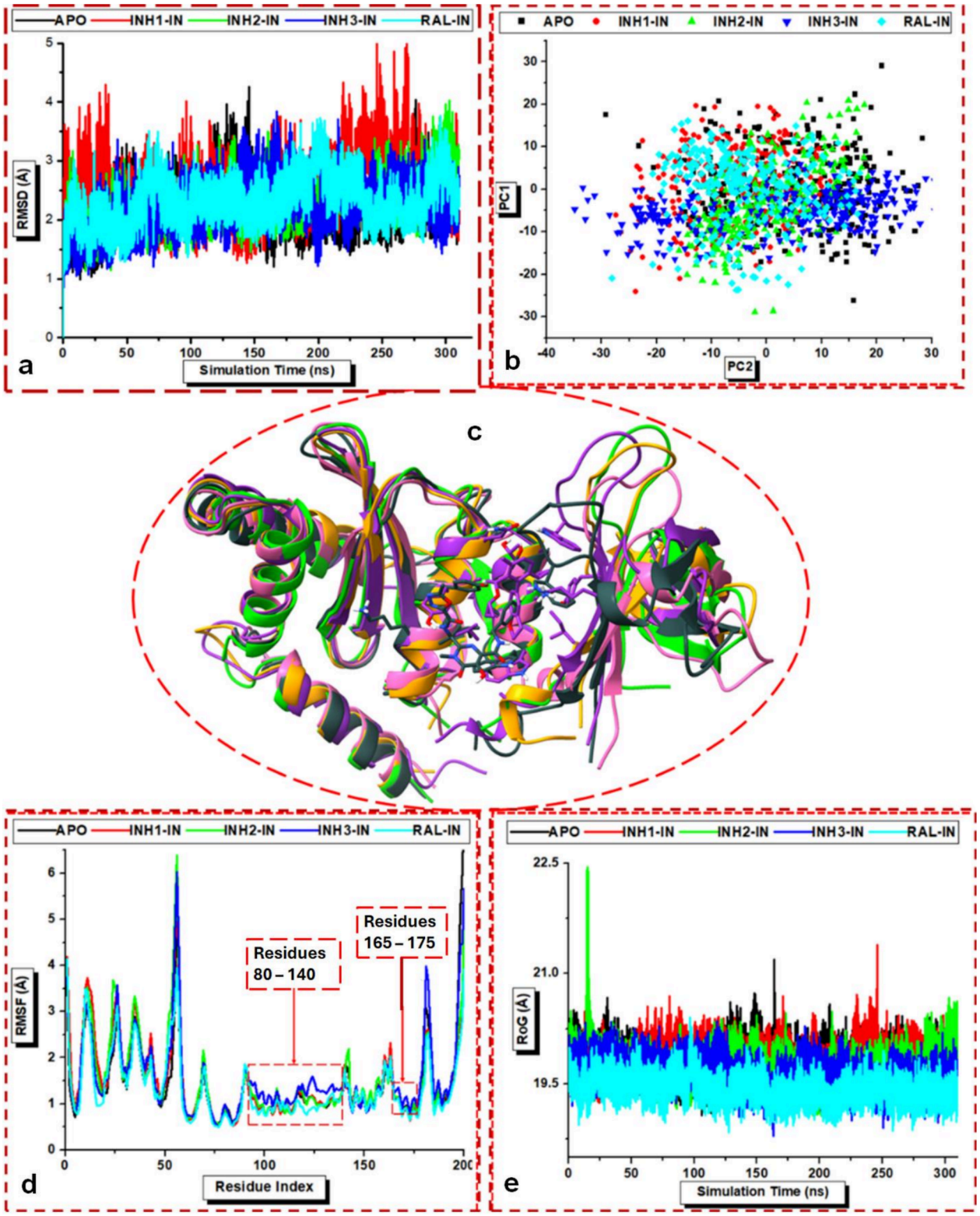


Figure 5

(A) The plots showing the RMSD, (B) RMSF, (C) The 2D PCA plot for the first two PC of the unbound IN (black), INH1-bound IN (red), INH2-bound IN, INH3-bound IN, and INH4-bound IN conformations sampled throughout simulated 200 ns followed using colour bars, (D) RoG, and (E) superimposed bound and unbound systems at 310 ns MD simulations. The boxes in B indicate the residues with erratic fluctuations in the INH3-bound and RLT-bound systems.

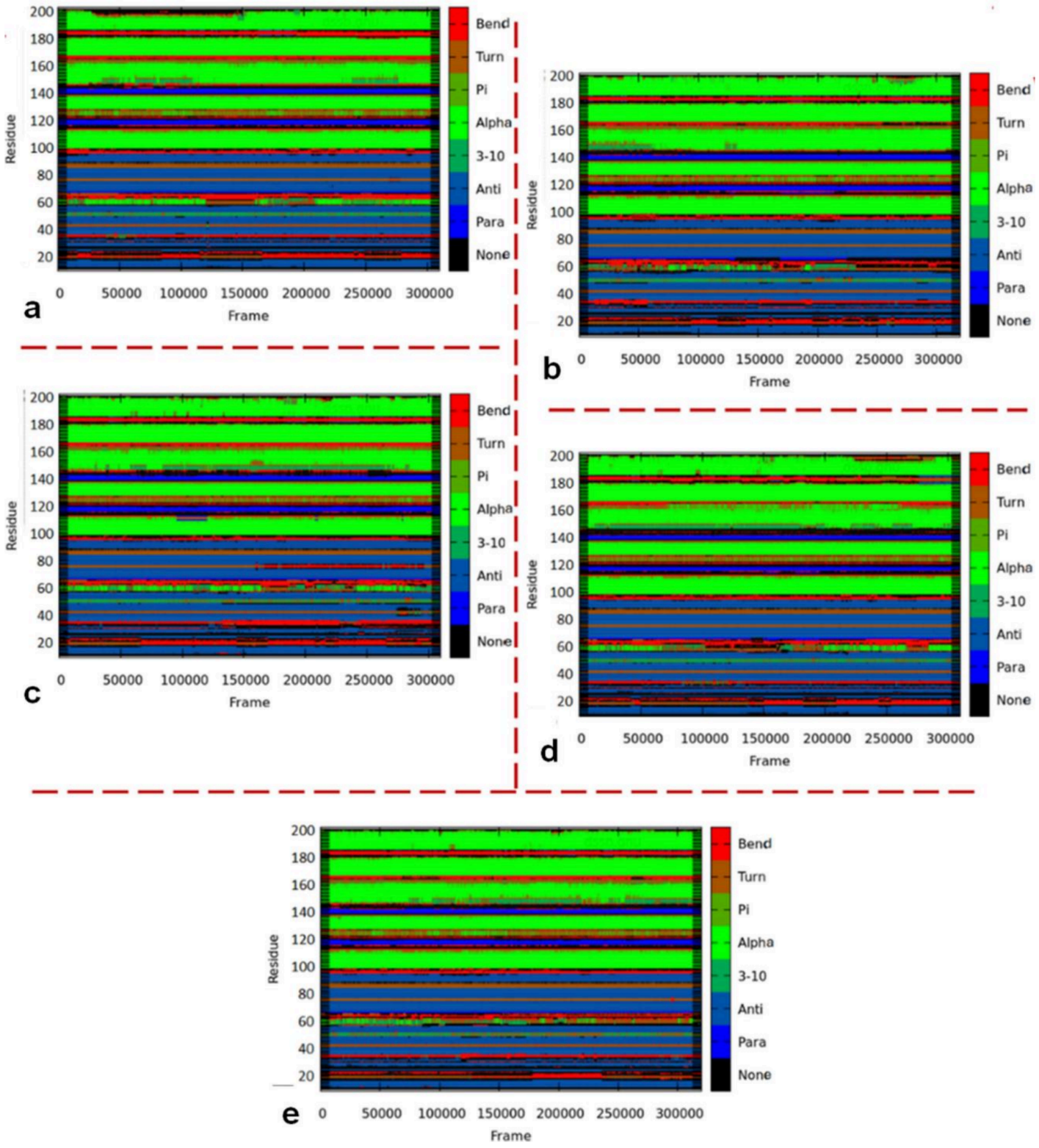


Figure 6

The DSSP charts for the unbound and bound HIV-1 IN CCD-CTD protein taken throughout 310 ns MD simulations; (a) unliganded protein, (b) INH1-bound HIV-1 IN, (c) INH2-bound HIV-1 IN, (d) INH3-bound HIV-1 IN, and (e) INH4-bound HIV-1 IN.

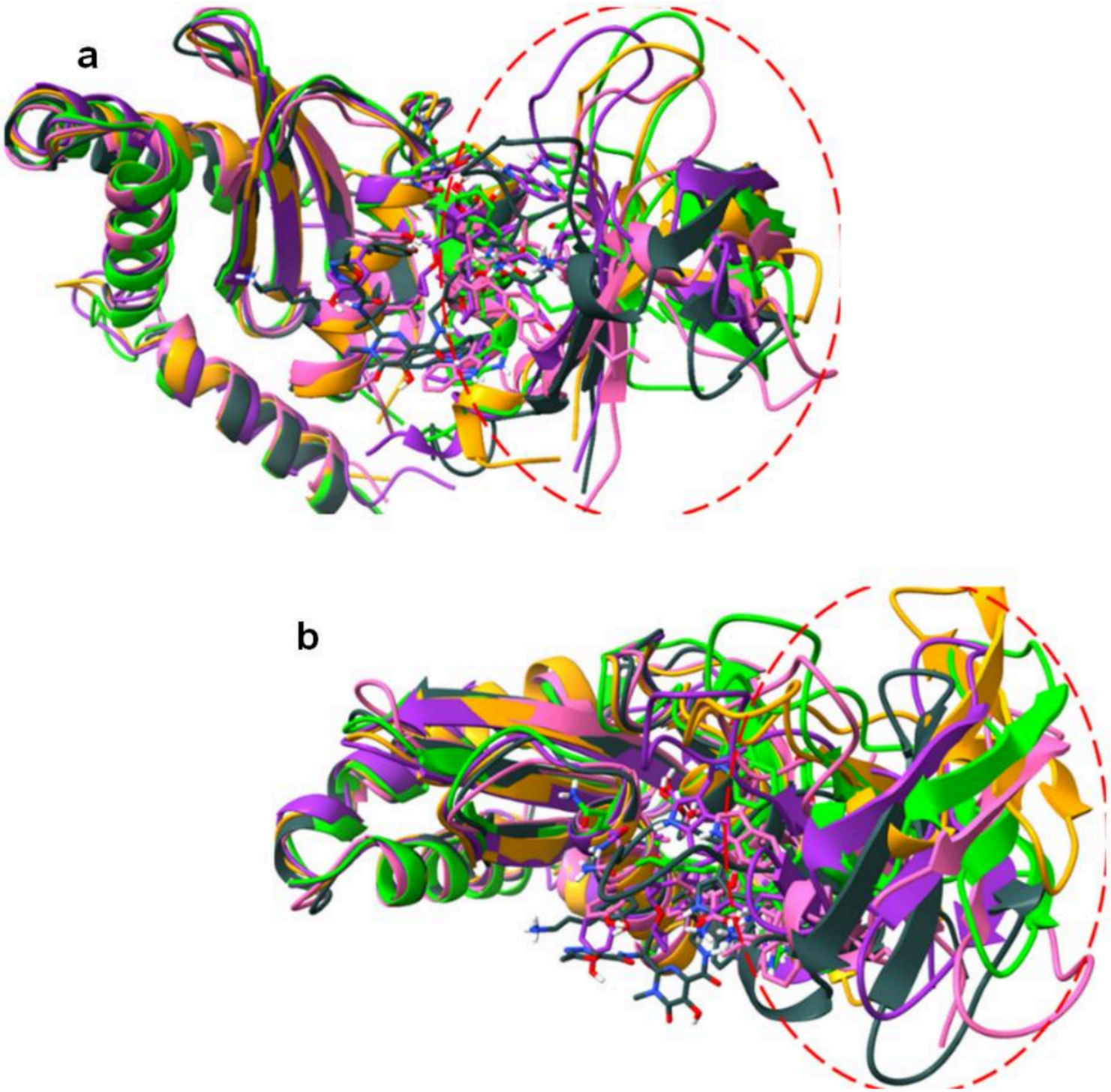


Figure 7

Superimposed Structures of Apo, INH_1-, INH_2-, INH_3-, and INH_4-bound HIV-1 IN CCD-CTD enzyme, showing the twisting, coiling, and unfolding transitional behaviour of the structures after MD simulations. (a) front structural view and (b) back structural view. Colour online: Apo (gold), INH1-bound IN (green), INH2-bound IN (magenta), INH_3-bound IN (purple), and INH_4-bound IN (dark slate grey).

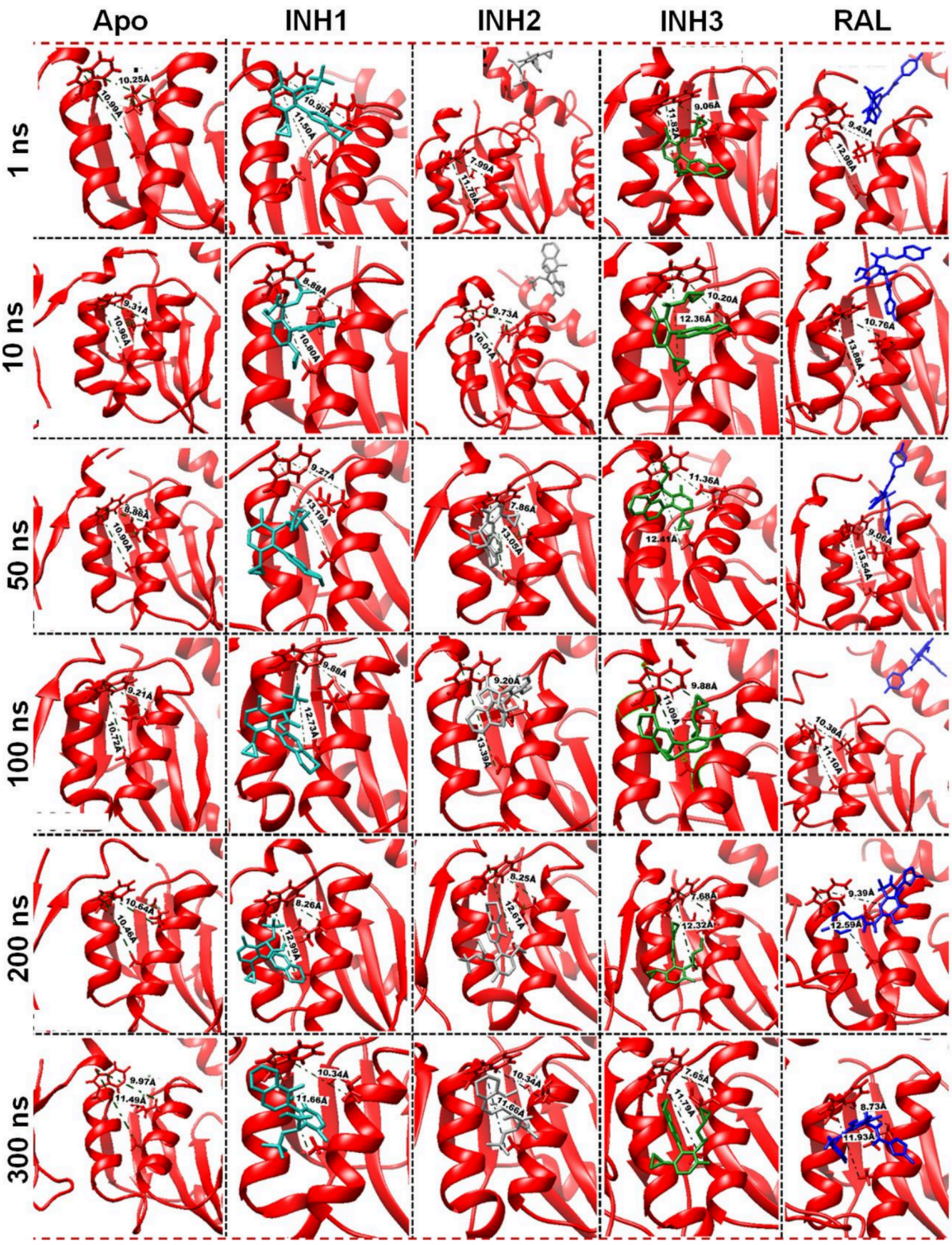


Figure 8

Showing the distances between interacting amino acids Trp132-Leu102 and Trp132-Ala98 in the apo and ligand-bound HIV-1 IN: INH1 (Cyan), INH_2 (grey), INH_3 (green), RAL (blue).

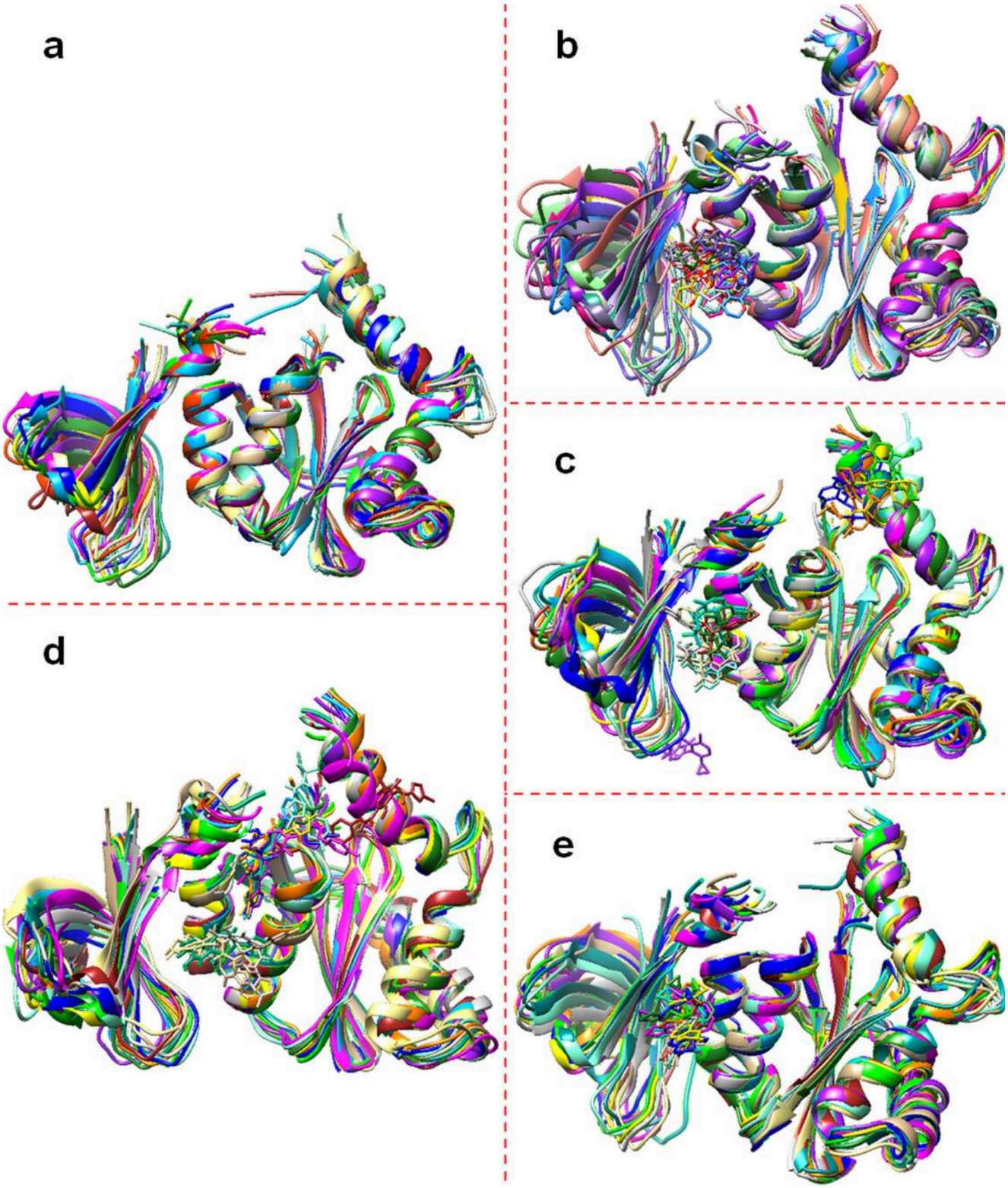


Figure 9

Showing a superimposed image of the unbound structure and bound integrase CCD-CTD complexes during 310 ns MD simulations. The visual images revealed significant differences across the systems. Colour outline: 1 ns (yellow), 2 ns (green), 5 ns (blue), 10 ns (orange), 15 ns (magenta), 20 ns (purple), 25 ns (forest green), 50 ns (deep sky blue), 100 ns (brown), 150 ns (acquamarine), 200 ns (tan), 250 ns (dark cyan), 300 ns (khaki), 310 ns (gray).